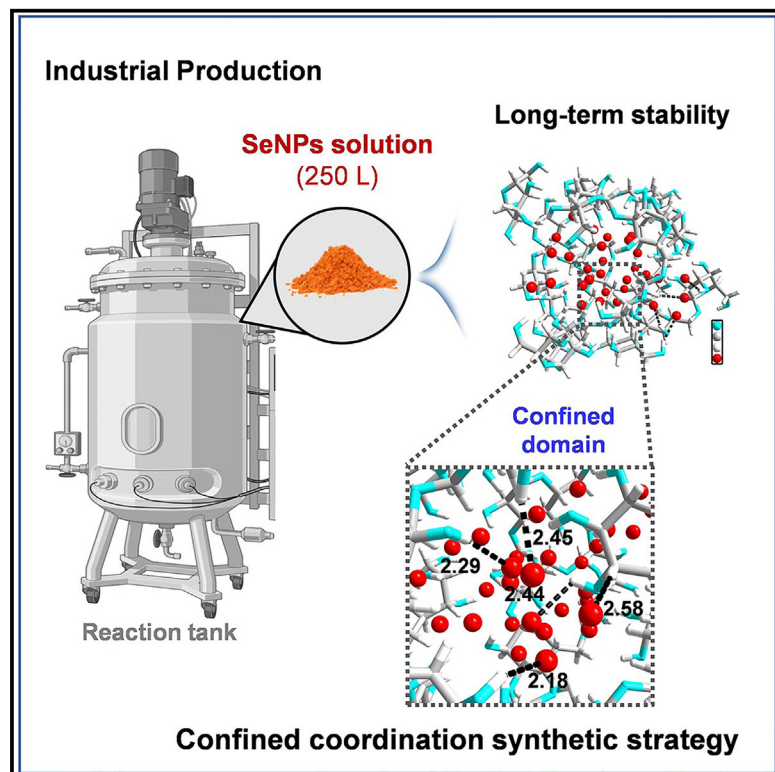


Industrial-level production of ultrastable selenium nanoparticles using a confined coordination synthetic strategy

Graphical abstract



Authors

Lizhen He, Zehang Zhang,
Zhiying Tang, ..., Lan Zheng,
Zushuang Xiong, Tianfeng Chen

Correspondence

xiongzs22@jnu.edu.cn (Z.X.),
tchentf@jnu.edu.cn (T.C.)

In brief

He et al. propose a confined coordinated strategy to control the formation process and structural stability of selenium nanoparticles for large-scale production and long-term preservation. The findings of the nucleation and growth process may provide important practical guidance for future fabrication and industrialization of inorganic nanomedicines.

Highlights

- Confined coordination is a key factor for selenium nanoparticle formation
- Lentinan confinement circumvents the excessive aggregation of selenium atoms
- Industrial production and long-term stability of selenium nanoparticles are demonstrated



Article

Industrial-level production of ultrastable selenium nanoparticles using a confined coordination synthetic strategy

Lizhen He,¹ Zehang Zhang,¹ Zhiying Tang,¹ Kui Shen,¹ Chengcheng Sang,¹ Lan Zheng,¹ Zushuang Xiong,^{1,*} and Tianfeng Chen^{1,2,*}

¹Department of Neurology and Stroke Center of The First Affiliated Hospital, Department of Chemistry, State Key Laboratory of Bioactive Molecules and Druggability Assessment, MOE Key Laboratory of Viral Pathogenesis & Infection Prevention and Control, Jinan University, Guangzhou 510632, China

²Lead contact

*Correspondence: xiongzs22@jnu.edu.cn (Z.X.), tchentf@jnu.edu.cn (T.C.)
<https://doi.org/10.1016/j.xcrp.2024.102303>

SUMMARY

The chemical nature of the formation and aggregation behavior is an important factor affecting the structural stability of nanoparticles, which is also an important basis on which to promote their future industrial production and clinical translation. Herein, we report a confined coordinated strategy using lentinan to control the nucleation and growth kinetics of selenium nanoparticles, which yields kilogram-scale production and up to 4 years of stability. Mechanistic analysis uncovers that the strong intermolecular interactions of selenium atoms with the hydroxy-rich lentinan significantly slow down the nucleus formation and growth process of the nanoparticles. In addition, the confined domain of lentinan circumvents the excessive accumulation, coagulation, and phase transformation of selenium atoms, thereby enhancing the stability of selenium nanoparticles. The findings on nucleation and growth processes of the nanoparticles may provide guidance toward future fabrication and industrialization of inorganic nanoparticles.

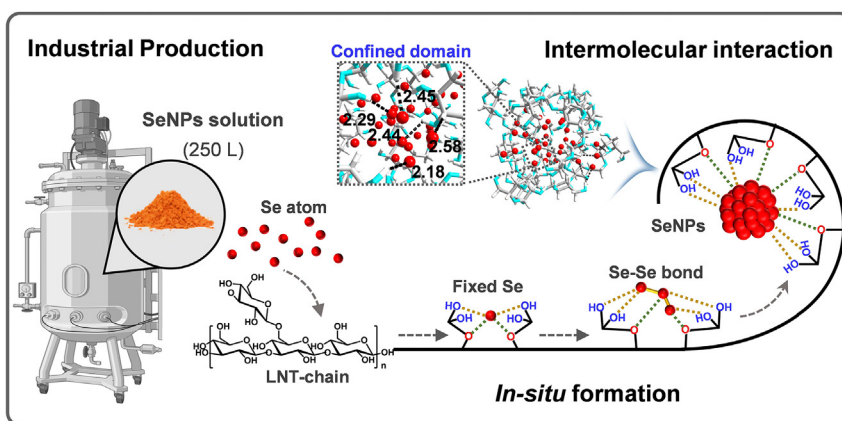
INTRODUCTION

The rapid development of nanotechnology has shown great promise in the fields of energy (biomedicines and catalysis), environment (pollution and water quality), and particularly biomedicines (nanomedicine, pharmacology, and biomedicine).^{1–3} However, the clinical translation and application of nanomedicines are usually hindered by a lack of nanomaterials that are highly efficient, have low toxicity, are easy to prepare, and have high potential druggability.⁴ On the other hand, there are difficulties in overcoming technological breakthroughs in the transition from laboratory research to industrial-scale production.⁵ These two bottlenecks have greatly restricted the advancement of nanomaterials from basic research to clinical application, posing a significant challenge in the field of nanomedicine. Specifically, a technological gap exists between the lab-developed and industrial manufacturing processes.⁶ For example, the lab-developed processes may involve complicated synthesis procedures, harsh conditions, and additional heating steps that are difficult to implement in industrial production. To bridge such a gap, it is essential to develop environmentally friendly and scalable manufacturing strategies. At present, a large amount of nanomedicine, such as multi-block polymers,⁷ organic-inorganic hybrid nanomaterials,⁸ multicomponent plasmonic nanoparticles (NPs),⁹ and metal-coordinated nanodrugs,¹⁰ exhibit significant anticancer efficiency, but their clinical application is limited due to the complex structures

and harsh synthesis requirements.¹¹ Therefore, the key to advancing the clinical adoption of nanomedicine lies in the development of nanomaterials with high bioactivity, clear structures, and convenient synthesis procedures.

To simplify the structures of nanomedicine, scientists have devoted great efforts to creating single-element NPs, including gold, silver, carbon, silicon, and selenium (Se). As a human essential trace element, Se stands out for its superior biocompatibility and biosafety compared to other elements, making selenium NPs (SeNPs) particularly promising for clinical translative potential.¹² SeNPs play key nutritional functions in supporting human health by converting to selenocysteine and inserting into selenoproteins, which help modulate redox balance and immune response.¹³ Based on their impressive physicochemical properties, SeNPs have been intensively investigated in various fields such as biomedicine (anti-tumor,¹⁴ anti-oxidation,¹⁵ immune regulation,¹⁶ etc.¹⁷), agriculture (selenium-enriched feed,¹⁸ fertilizer,¹⁹ soil,²⁰ etc.), food (selenium-enriched milk,²¹ eggs and rice,²² etc.), healthcare,²³ and so on. To meet the huge market demand, it is imperative to develop efficient and environmentally friendly methods to ensure large-scale production of SeNPs with uniformity in size, morphology, and chemical composition. Different synthesis approaches, including physical, chemical, and biological methods, to fabricate SeNPs have been explored.¹⁴ Physical synthesis (like delamination, laser etching, and hydrothermal/solvothermal syntheses) usually results in ununiformed particle sizes and poor dispersity,²⁴





Scheme 1. Illustrated diagram of confined coordinated strategy for formation and industrial production of SeNPs

RESULTS

LNT prevents SeNPs from undergoing crystalline phase transformation

The potential supramolecular interactions between the side chains of polysaccharides and the Se atoms, on the one hand, hinder the bond formation and oriented attachment of Se atoms to inhibit the crystallization and, on the other

while biosynthesis (microbiome fermentation, plant extract synthesis) is of low yield and difficult to execute on a large scale.²⁵ Chemical synthesis through the reduction of sodium selenite (selenium source, Na_2SeO_3) with ascorbic acid (vitamin C [VC], reducing agent) is currently the primary strategy for laboratory-scale production²⁶ and has the potential for large-scale application.²⁷ However, due to the amorphous state, high free energy, high surface energy, and low glass transition temperature (48°C – 50°C) of SeNPs,²⁸ challenges such as aggregation, phase transition, and stability enhancement need to be addressed before successful industrialization.

Currently, the synthesis strategies for highly stable nanomaterials include synthetic condition adjustment (reaction temperature, time, reactants molar ratio),²⁹ structure optimization (particle size, shape, defect),³⁰ surface modification (solvation, functionalization, etc.), interfacial-confined coordination³¹ (reverse micelle process as an example^{32,33}), and *in situ* surface modification (adding polymers,³⁴ biomacromolecules;³⁵ polysaccharides,³⁶ and other modifiers during synthesis³⁷). Polysaccharides are particularly attractive for stabilizing NPs due to their biocompatibility, biodegradability, low cost, and abundant functional groups. Meanwhile, the supramolecular interactions and self-assembly structure of polysaccharides decrease the surface and free energy of the nucleus, thus stabilizing the NPs.³⁸ Despite the extensive research on the synthesis of SeNPs using polysaccharides, the industrialization process remains slow, and the stabilization mechanism of polysaccharides on SeNPs is not fully understood. This study aims to uncover the mechanism of polysaccharide modification to confine the coordination between the polysaccharide with SeO_3^{2-} and Se atoms for industrial production and long-term storage of SeNPs. We have scaled up the reaction volume for preparation of SeNPs to pilot scale and 250 L-industrial scale. We discovered the unique performance of a polysaccharide, lentinan (LNT), in *in situ* regulating the nucleation and growth kinetics, preventing phase transformation, and stabilizing SeNPs through confined coordination of hydrogen bonds and van der Waals interactions with SeO_3^{2-} and Se atoms. This study not only elucidates the critical role of confined coordination structure of LNT in regulating the nucleation, growth, and stability of SeNPs, but also provides important scientific basis and guidance for future fabrication of other nanomedicines (Scheme 1).

hand, decreases the surface energy to stabilize the SeNPs. Meanwhile, the hydrophilic/hydrophobic domains in the self-assembly structure of polysaccharides could absorb the Se atoms to further decrease the free energy of the Se crystal nucleus.³⁹ Hence, in order to improve the stability and inhibit the crystallization process of amorphous SeNPs, we selected three typical polysaccharides, LNT, poria cocos mushroom polysaccharide (CMP), and chitosan (CS), to investigate their stabilizing effects on SeNPs. Initially, we examined the morphology and chemical structure changes of polysaccharide-modified SeNPs (CS@SeNPs, CMP@SeNPs, and LNT@SeNPs) over 40 days. The elemental mapping results showed that the main signals of Se appeared in the three NPs of LNT@SeNPs, CS@SeNPs, or CMP@SeNPs. Furthermore, the O signals from the polysaccharide, especially the N signals from CS, were also completely colocalized in the NPs of LNT@SeNPs, CMP@SeNPs, and CS@SeNPs, which confirmed the success modification of polysaccharide (Figure S1). Subsequently, the pictures of the aqueous solution in Figure 1A show that LNT@SeNPs remained homogeneous over 40 days, while the aqueous solutions of CMP@SeNPs and CS@SeNPs exhibited varying degrees of stratification and precipitation, with CS@SeNPs showing the most significant changes. This phenomenon directly verifies that the stability of LNT@SeNPs is significantly higher than that of CMP@SeNPs and CS@SeNPs. Transmission electron microscopy (TEM) analysis revealed that there were no noticeable morphology changes in LNT@SeNPs during the 40 days. In contrast, both CS@SeNPs and CMP@SeNPs began to gather and agglomerate after 10 days, forming block-shaped structures over time. This result further confirms the stability of LNT@SeNPs and the tendency of CMP@SeNPs and CS@SeNPs to undergo crystalline phase transformation. Meanwhile, dynamic light scattering (DLS) measurements showed that the size of CS@SeNPs increased dramatically to 900 nm after 20 days, eventually reaching 1,400 nm (Figure 1B), which is completely consistent with the results of the average diameter in TEM images. The size of CMP@SeNPs was found to increase from 180 to 400 nm, while LNT@SeNPs showed only a slight fluctuation in particle size (Figure S2). This tendency completely agreed with the polydispersity index (PDI) value in Figure S3. These

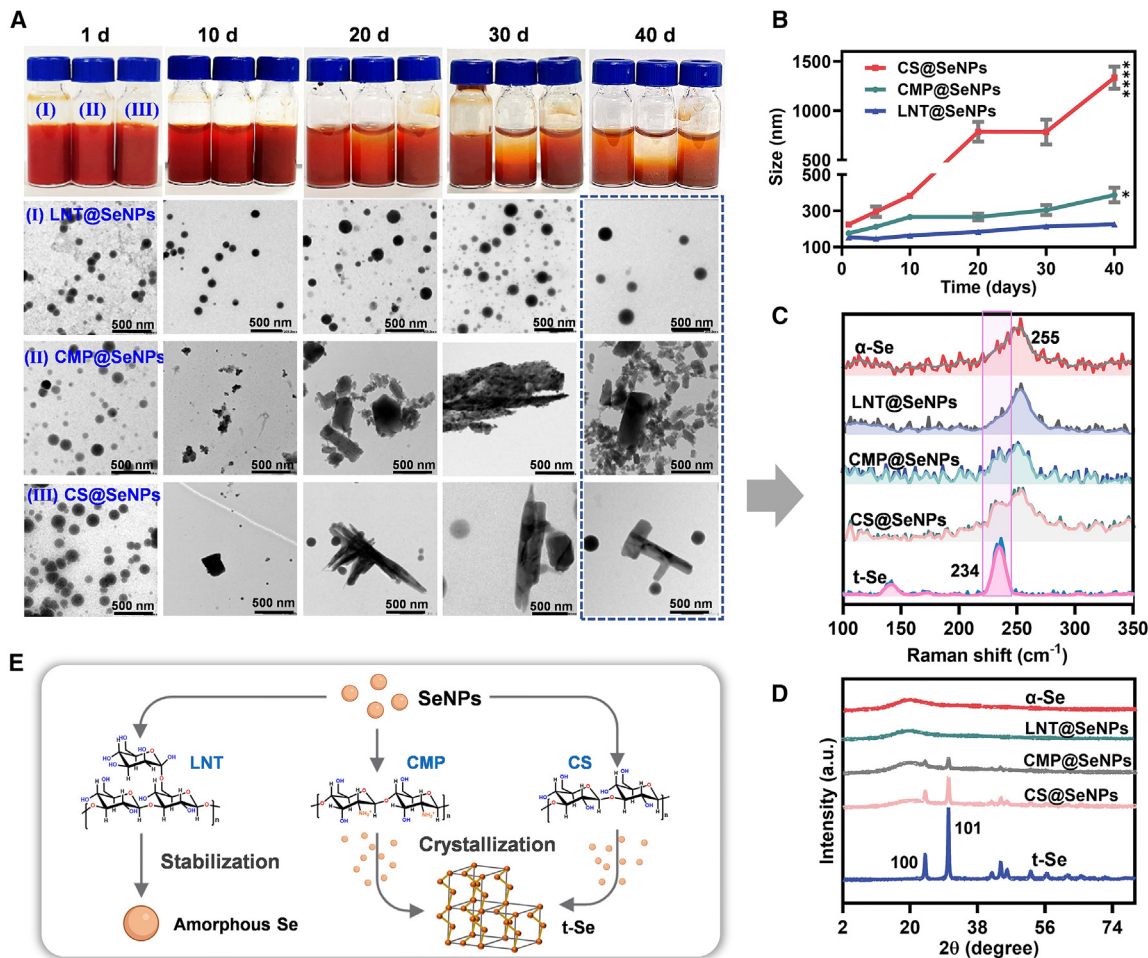


Figure 1. Regulation phase transformation of SeNPs

(A) Pictures and TEM images of LNT@SeNPs, CMP@SeNPs, and CS@SeNPs in aqueous solutions during the 40 days. The scale bars in TEM images represent 500 nm. See also Figure S2.

(B) Size fluctuation of LNT@SeNPs, CS@SeNPs, and CMP@SeNPs in aqueous solutions within 40 days ($n = 3$, $*p < 0.05$, $***p < 0.0001$, compared with LNT@SeNPs). Data are represented as mean \pm SD. The size distribution was measured at 25 °C.

(C and D) Raman spectra (C) and PXRD patterns (D) of SeNPs with different polysaccharides after 40 days.

(E) Illustration of three polysaccharides stabilizing SeNPs and preventing phase transformation. LNT@SeNPs, CS@SeNPs, and CMP@SeNPs were dispersed in aqueous solutions (8 mmol L⁻¹), and Raman spectra and PXRD patterns were collected after 40 days.

results confirmed the stability of LNT@SeNPs and the aggregation of CS@SeNPs and CMP@SeNPs. In order to gain more insight into the changes of the systems, Fourier Raman spectroscopic analysis was implemented. Raman spectra revealed a sharp peak at 234 cm⁻¹ in the spectrum of crystalline Se (t-Se), which also appeared in the spectra of CS@SeNPs and CMP@SeNPs after 40 days, indicating a phase transition (Figure 1C). On the other hand, no characteristic peaks of t-Se were observed in the Raman spectrum of LNT@SeNPs, suggesting that LNT prevents the crystalline phase transformation of SeNPs compared to CS and CMP. Consistently, powder X-ray diffraction (PXRD) data showed the appearance of characteristic (100) and (101) crystal faces of t-Se in CS@SeNPs and CMP@SeNPs (Figure 1D), further ascertaining a phase transition from amorphous to crystalline Se.⁴⁰ In contrast, no

typical diffraction of crystalline Se was observed in the PXRD pattern of LNT@SeNPs, demonstrating its high stabilizing effects. All these results suggest that LNT prevents SeNPs from undergoing crystalline phase transformation to enhance its stability. The difference in the stability of polysaccharide-modified SeNPs may be attributed to their varying chemical structures, with LNT's glucan main chain and glucose side chains potentially playing a key role in stabilizing SeNPs (Figure 1E). It is proposed that the strong supramolecular interactions between LNT and SeNPs decrease the interfacial energy of SeNPs, thus impeding the aggregation and phase transformation. As regulating the phase transformation process is crucial for large-scale nanomaterial production, such a unique property makes LNT an ideal candidate for industrial production and long-term storage of SeNPs.

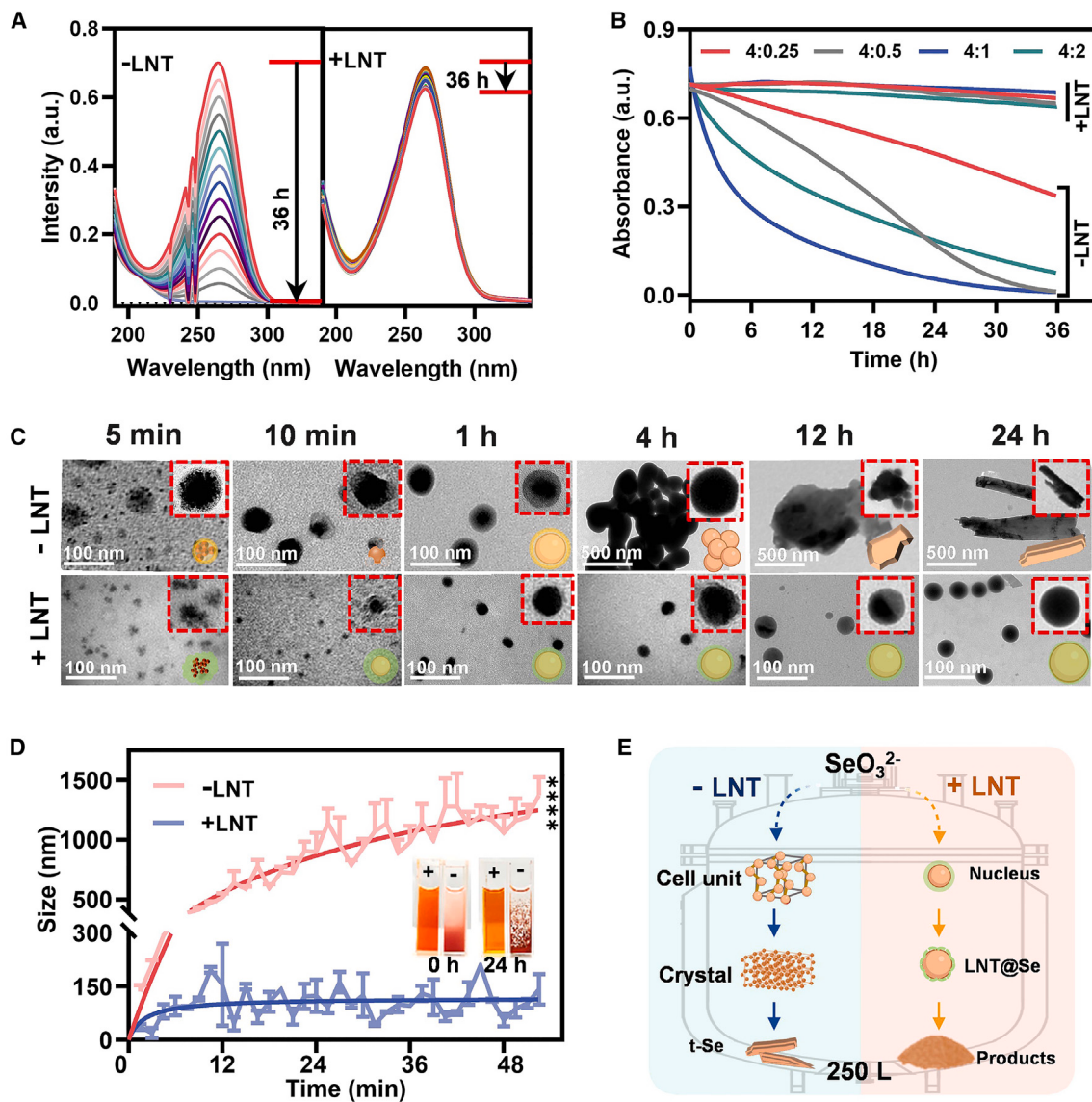


Figure 2. Nucleation and growth kinetics of SeNPs with or without LNT

(A) UV-vis spectra of the reaction systems with or without LNT (50 mg L^{-1}). The concentrations of VC and Na_2SeO_3 are 12.5 and $50 \mu\text{mol L}^{-1}$, respectively, and the absorption data from 190 to 350 nm were collected every 5 min for 36 h .

(B) Time-dependent absorption intensity for reaction system of VC and Na_2SeO_3 . The concentration of Na_2SeO_3 is 1.0 mmol L^{-1} and remains fixed. The ratios of VC to Na_2SeO_3 are $4:0.25$, $4:0.5$, $4:1$, and $4:2$.

(C and D) TEM images (C) and particle size (D) for the reaction systems of Na_2SeO_3 and VC with or without LNT (50 mg L^{-1}) at different time points ($n = 3$, *** $p < 0.0001$, compared with +LNT). Inset: pictures for solutions of LNT@SeNPs (+) and naked SeNPs (-) at the beginning of the reaction and 24 h after the reaction. The concentrations of Na_2SeO_3 and VC are 2.0 and 8.0 mmol L^{-1} , respectively.

(E) Schematic illustration of LNT controlling the nucleation and growth process of SeNPs.

LNT controls the nucleation and growth kinetics of SeNPs

The nucleation and growth processes play important roles in changing the chemical structure to regulate the stability of nanomaterials.⁴¹ We further evaluated the impact of polysaccharides on the nucleation and growth speed of SeNPs. Firstly, we used UV-visible (UV-vis) to monitor the reaction between SeO_3^{2-} and VC and observed a significant decrease in the absorption in-

tensity of VC at 267 nm within 36 h (Figure 2A). This result indicated a quick reaction between Na_2SeO_3 and VC, while the presence of LNT slowed down the reaction rate and the formation of SeNPs, as evidenced by a slower decrease in absorption. Additionally, compared with the reaction system containing LNT, the reaction time of SeNPs without LNT modification rapidly decreased with the increase of the molar ratio of VC: Na_2SeO_3 (Figure 2B). These results imply that LNT slows down the

reaction between Na_2SeO_3 and VC. TEM analysis revealed differences in the nucleation process of SeNPs with or without LNT. As shown in Figure 2C, SeNPs (the nucleus) were quickly formed at the early stage of the reaction (about 5 min) without LNT (naked SeNPs), and particle size gradually increased within 1 h. Then, the NPs aggregated at 12 h. In contrast, SeNPs in the presence of LNT showed much smaller cluster structures in 5 min. The particles did not increase as dramatically as the system without LNT within 24 h. Similarly, DLS measurements showed that the particle size of naked SeNPs increased from 200 to 1,600 nm in 2 h, while the particle size for reaction systems in the presence of LNT remained constant (approximately 100 nm). What's more, the picture of the reaction solution clearly showed that precipitation occurred in the reaction system without LNT at 24 h, while the reaction mixture solution containing LNT remained homogeneous (Figure 2D). All these results indicated that LNT can indeed slow down the nucleation and aggregation processes of Se atoms, facilitating the industrial production of stable SeNPs (Figure 2E). Based on the agglomeration and crystal transformation caused by the high disorder and surface energy of amorphous NPs, it is proposed that the weak interaction between LNT and Se atoms reduced the interfacial energy of SeNPs, contributing to the stability of LNT@SeNPs.⁴²

Confined coordination of LNT for *in situ* nucleation of SeNPs

To further investigate the chemical nature of polysaccharides to regulate the nucleation and growth kinetics and thus stabilize SeNPs, molecular dynamics (MD) simulations were performed to model the interaction between SeO_3^{2-} and LNT using density functional theory (DFT) calculations. As shown in Figure S4, the energy and temperature for system of LNT and SeO_3^{2-} decreased in a time-dependent way. After 100 ps of simulation at 298 K, a balance was reached. These results revealed a spontaneous interaction of SeO_3^{2-} with LNT. Furthermore, as shown in Figure S5, snapshots of the evolution process showed that, at 0 ps, the helical LNT aggregated into a hollow circular cluster, with the β -glucosyl group located outside of the main chain and the SeO_3^{2-} randomly distributed both inside and outside the circular cluster. In the dynamic process of 100 ps, the β -glucosyl branch of LNT twisted, flipped, and folded into a hollow spherical structure, with SeO_3^{2-} accumulated inside it. This tendency indicated that LNT restricted the movement of SeO_3^{2-} . In addition, interaction energy analysis reflected that the intermolecular van der Waals interactions between SeO_3^{2-} and LNT are the stable factors of the system (Figure 3A). This kind of non-covalent interaction impeded the reduction of SeO_3^{2-} by VC and reinforced the formation of SeNPs *in situ*. As the different performances in stabilizing SeNPs may be attributed to the interactions with SeO_3^{2-} , we detected the interaction between the three polysaccharides and LNT by isothermal titration calorimetry (ITC) analysis. The ITC responses signals confirmed that LNT and CMP had a stronger interaction with SeO_3^{2-} compared to CS, as evidenced by their positive heat deflection and stronger heat response (Figure 3B). Zeta potential measurements further supported this finding, showing a significant increase in the zeta potential for the mixture of SeO_3^{2-} and CS. This result indicated a weak interaction between SeO_3^{2-} and CS. On the contrary,

only slight fluctuations were observed in the system of LNT and CMP with SeO_3^{2-} , suggesting a stronger interaction consistent with the ITC results (Figure 3C). After being anchored in polysaccharide, SeO_3^{2-} is reduced by VC into Se atoms; hence, the interaction of Se atoms within the polysaccharide system is another crucial factor for the stability of SeNPs. To investigate this, we simplified the structures of the three polysaccharides (LNT, CMP, and CS) and studied the evolution process of Se atoms in the polysaccharides. The snapshot and video of the evolution process revealed that LNT formed a closed circle with Se atoms gathered inside, limiting their diffusion, while CMP and CS formed an open circle, causing the migration of partial Se atoms out of the polysaccharides (Figures 3D and S6; Video S1). This effect suggested that LNT not only restricted the movement of SeO_3^{2-} but also gathered the synthesized Se atoms. This unique structural advantage of LNT can be attributed to the presence of the β -(1-6)-linked glucosyl side chains in the main glucan chain that promotes the formation of a closed ring structure that restricts the movement of Se atoms SeO_3^{2-} with confined coordination. Based on the differences of these chemical groups, we then further explored their binding energy with Se atoms by analyzing the binding sites and binding energies. It was found that the interaction of Se atoms with LNT was much stronger than with CS and CMP (Figure 3E). Meanwhile, the abundance of binding sites (hydroxyl groups and ether O atoms) on the LNT chain, along with hydrogen bonding and van der Waals interactions, serve as the main driving force for LNT to stabilize the SeNPs (Figures 3F and 3G). Overall, the hydroxyl-rich closed circle structure of LNT allows it to effectively interact with Se atoms and SeO_3^{2-} by confined coordination, *in situ* regulate the nucleation, growth kinetics, and stability, and control the crystal phase transformation, leading to the successful large-scale synthesis of SeNPs.

LNT complexation assists with scale-up production of SeNPs

Based on the full understanding of the mechanism for LNT to control the nucleation and growth process and prevent the crystalline phase transformation of SeNPs, we commenced to industrialize the production of LNT@SeNPs through a stepwise scale-up reaction process from the laboratory to industrial scale (Figure 4A). By successfully preparing the three types of polysaccharide-modified SeNPs in laboratory- (100 mL) and pilot-scale (5.0 L) experiments, we found that although the particle sizes remain below 150 nm, only LNT@SeNPs exhibited high stability when the reaction was scaled up to 250 L (industrial production) (Figure 4B). This phenomenon indicated that LNT may be the preferred choice for industrializing SeNPs. Furthermore, a comparative analysis of the size and zeta potential at various concentrations of modified SeNPs showed significant fluctuation in these properties for CS@SeNPs and CMP@SeNPs, while LNT@SeNPs remained stable, suggesting its suitability for high-concentration SeNP preparation (Figure 4C; Table S1). Additionally, the particle size of LNT@SeNPs remained consistent throughout the scale-up process (Figure 4D), ascertaining the feasibility of SeNP industrialization. Hence, we carried out the industrial production of SeNPs (at a reaction concentration of 32 mmol L⁻¹) with LNT from laboratory to pilot to industry scale

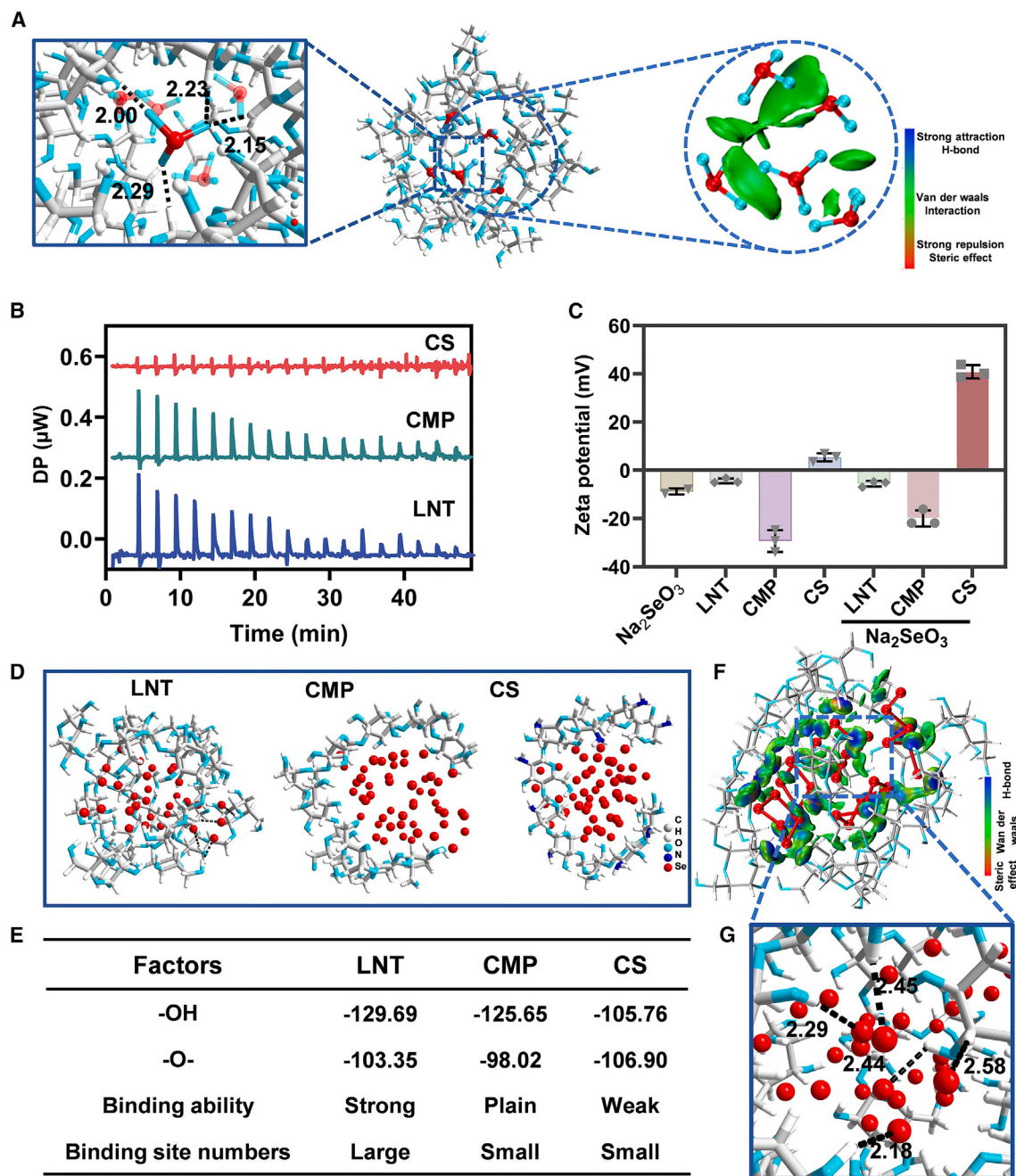


Figure 3. Studies of interactions of polysaccharides with SeO_3^{2-} and Se atoms

(A) Snapshot of the evolution process of SeO_3^{2-} and LNT at 100 ps. See also Figure S5.

(B and C) ITC curves (B) and zeta potentials (C) for the mixtures of polysaccharides and SeO_3^{2-} . The concentrations of Na_2SeO_3 and polysaccharides are 4.0 mmol L^{-1} and 4.0 mg L^{-1} , respectively. Data are represented as mean \pm SD.

(D) Representative structures for the systems of polysaccharides and Se atoms in the dynamic process within 100 ps. See also Figure S6.

(E) Table of binding energy for Se atoms at different sites. The unit is kcal mol^{-1} .

(F and G) The intermolecular noncovalent interaction based on independent gradient model (IGM) (F) and interaction sites (G) of LNT and Se atoms. Hydrogen atoms of LNT are omitted for clarity (color code: red = Se, cyan = O, gray = C, and cyan = O in SeO_3^{2-}).

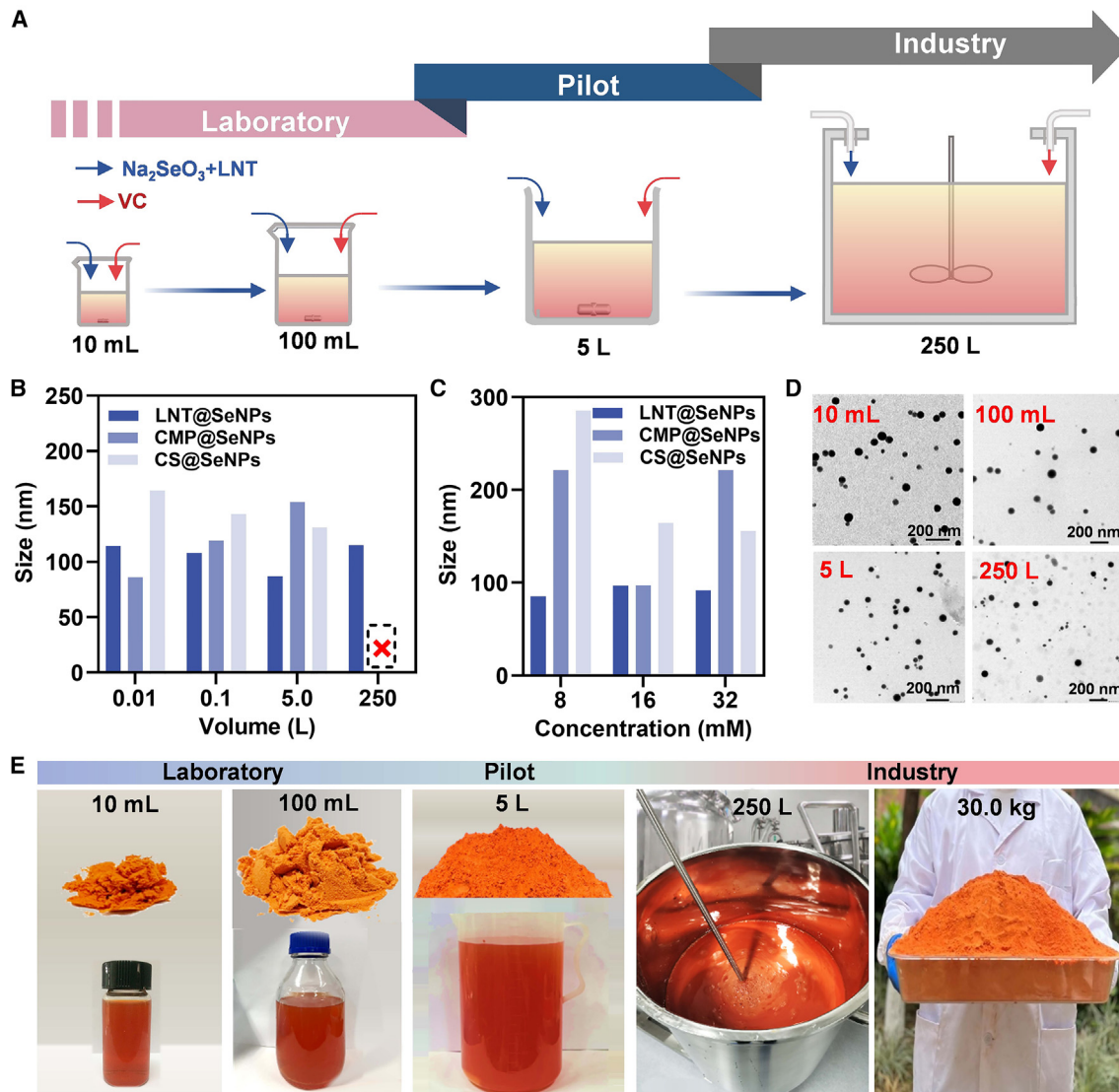


Figure 4. Scale-up production of SeNPs in the presence of LNT

(A) Schematic illustration of scale-up production of SeNPs.

(B and C) Size distribution of LNT@SeNPs, CS@SeNPs, and CMP@SeNPs at different scales (B) and concentrations (C). The reaction concentration is defined as the initial concentration of Na_2SeO_3 .

(D) TEM images of SeNPs from different reaction scales. The scale bars represent 200 nm.

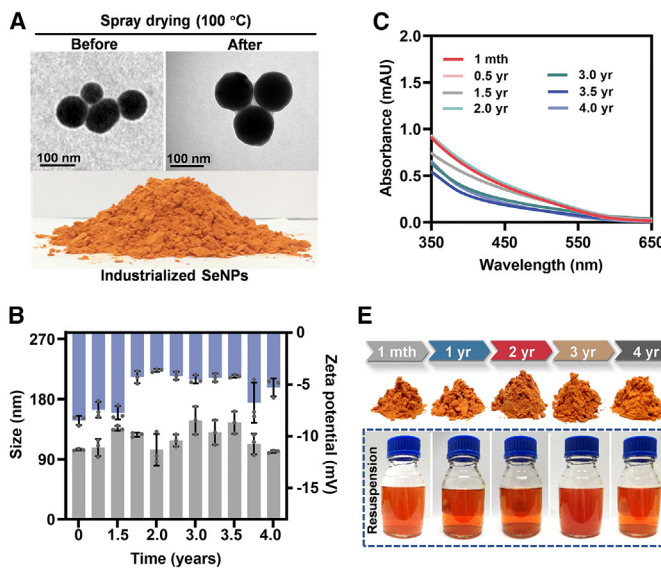
(E) Pictures of SeNP reaction solutions at different scales and the corresponding powder products. The reaction concentration is 32 mmol L^{-1} , and the powder products are after freeze drying or spray drying.

(Figure 4E). The obtained LNT@SeNPs in the 250 L industrial preparation were further characterized by TEM, and the results show the uniform dispersion of spherical NPs with a size of approximately 100 nm (Figure S7). These results confirm the superior performance of LNT in chemical engineering and industrial production of SeNPs.

Long-term stability analysis of the industrial SeNPs

Spray drying is commonly used in industry to dry samples for transport and long-term storage.⁴³ In this study, the LNT@SeNP solution was spray dried in the presence of maltodextrin to pre-

vent agglomeration and adhesion. Approximately 30 kg (with 300 g elemental Se) of industrial LNT@SeNP powder was produced using a rotary spray drying tower. We evaluated and found that the morphology of LNT@SeNPs remained unchanged before and after spray drying, suggesting the preservation of the structure of LNT@SeNPs (Figure 5A). Additionally, the particle size and surface zeta potential of the LNT@SeNPs showed minimal changes after spray drying, further confirming the structural stability of the LNT@SeNPs during the process (Figure S8). Moreover, long-term storage is inevitable for industrial NPs, and our assessment revealed that the particle size and surface potential



of the LNT@SeNPs remained constant over 4 years, with a fluctuation ratio within $\pm 20\%$ (Figure 5B). Consistent vis spectra (Figure 5C) and TEM images (Figure 5D) further confirmed the stability of LNT@SeNPs over time. What's more, pictures of the obtained SeNP powder and solution after resuspension showed no obvious changes (Figure 5E), consistent with the results from TEM, DLS, and vis absorption. Overall, these results suggested that the industrial SeNPs maintained remarkable stability during spray drying and long-term storage of 4 years.

DISCUSSION

Although the potential application of nanomedicine has attracted great attention, the transition from laboratory research to industry production remains a challenge due to challenges in technical optimization, stability and quality control, reproducible production processes, and long-term storage. SeNPs are a promising nanosystem for industrialization and clinical translation, profiting from low toxicity and high bioactivity. In this study, we develop a confined coordinated strategy to stabilize SeNPs by screening polysaccharides and chose LNT as the preferred choice for laboratory, pilot, and industry production of SeNPs. Overall, LNT controls the nucleation and growth kinetics and prevents the crystalline phase transformation of SeNPs. We realize not only kilogram-scale and 250 L volume production but also the long-term (up to 4 years) stability of the SeNPs. Short-term stability analysis shows that LNT remarkably enhances the stability of SeNPs to avoid agglomerate and crystalline phase transformation. Reaction process monitoring further reflects that LNT could effectively slow down nucleation and growth. The underlying mechanism confirms that LNT interacts with SeO_3^{2-} and Se atoms through confined coordination. Intramolecular interaction analysis ascertains that the unique structure of LNT, the β -(1-6)-linked glucosyl side chains, and the abundance of ether O atoms and hydroxyl groups provide the enhanced stabilization of

Figure 5. Stability of the industrial SeNPs during spray drying and long-term storage

(A) TEM images of SeNPs before and after the spray drying as well as a picture of the obtained products. The scale bars represent 100 nm.

(B and C) Size and zeta potential fluctuation (B) and UV-vis absorption (C) of the industrial LNT@SeNPs over 4 years. The concentration of LNT@SeNPs for UV-vis spectroscopic measurement is 8.0 mmol L $^{-1}$. Data are represented as mean \pm SD.

(D) TEM images of the industrial SeNPs over 4 years. The scale bars represent 100 nm.

(E) Pictures of the as-prepared SeNP powders and solutions after resuspension over 4 years. mth; month; yr, years.

SeNPs through hydrogen bonding and van der Waals interactions between the confined domain and Se atoms. Taken together, we elucidated the critical role and chemical nature of LNT in *in situ* regulating the nucleation, growth, and stability of SeNPs. Importantly, this study marks a breakthrough as a pioneered trail for large-scale production and elucidation of the formation mechanism of SeNPs, which may provide very important scientific basis and clear guidance for future fabrication of other nanomedicines. For future works, more efforts should be committed to the clinical transformation and application, biological molecular mechanisms, and synthetic process optimization of SeNPs in the nanomedicine field.

EXPERIMENTAL PROCEDURES

Materials and instruments

Na_2SeO_3 (99%) and VC (99%) were purchased from Sigma-Aldrich. LNT (96%), CS (with degrees of deacetylation $\geq 95\%$), and CMPs (80%) were obtained from Shanghai Yuanye Bio-Technology. Nitric acid (HNO_3 , 68%) and hydrochloric acid (HCl, 36%–38%) were obtained from the Guangzhou Chemical Reagent Factory. Deionized water with a resistivity of 18.25 M Ω cm was achieved using the Millipore Milli-Q Advantage A10 system.

Short-term stability observation of SeNPs

4.0 mg L $^{-1}$ aqueous solution of LNT was used to dissolve VC and Na_2SeO_3 to be a solution with concentrations of 30 and 15 mmol L $^{-1}$, respectively. 20 mL VC solution was slowly dropped into Na_2SeO_3 , and the mixture was gently stirred overnight. Then, the reaction solution was dialyzed with dialysis tubes (10 kDa, Millipore) in ultrapure water for 24 h. The prepared SeNPs were nitrified with a mixed acid of hydrochloric acid and nitric acid (volume/volume = 3:1) and quantified with inductively coupled plasma mass spectrometry (Thermo Scientific, iCAP RQ). 1 mL NPs in glass vials were kept at room temperature before pictures were taken at the time points of 1, 10, 20, 30, and 40 days. Meanwhile, the NP size was measured by DLS analysis (Malvern, NANO ZS), and about 20 μL solution was dropped onto TEM grids for TEM observation (Hitachi H-7650, 100 kV). The sediment of SeNPs at the time point of 40 days was separated for Raman spectra (HORIBA, LabRAM HR Evolution) and PXRD (Bruker, D8 advance) analysis. The results of Raman spectra were analyzed and exported by LabSpec 6. PXRD data were measured from 2° to 80° at a scan speed of $10^\circ \text{ min}^{-1}$ and a step of 0.02° . The data of the particle size distribution were exported from ZETASIZER SOFTWARE v.7.12. The size fluctuation curves were drawn with GraphPad Prism 8.3.0. The collected data of Raman spectra and PXRD were exported in TXT format and visualized with GraphPad Prism 8.3.0.

Monitoring of the reaction system in the formation of SeNPs

The dynamic process of the reaction was monitored by UV-vis spectra (Agilent, Cary 3500), TEM, and DLS analysis. Stock solutions of VC and Na₂SeO₃ were prepared at concentrations of 8.0 and 2.0 mmol L⁻¹, respectively. The maximum absorption of the reaction was adjusted to 0.8 (where the concentration of VC was around 12.5 μmol L⁻¹). Absorption spectra were recorded from 190 to 350 nm. The reaction was implemented first without LNT, and the absorption spectra of the mixture were recorded every 5 min until the absorption intensity at 267 nm decreased to 0 (about 36 h). As a comparison, the reaction with LNT (LNT concentration: 50 mg L⁻¹) was monitored under the same conditions for about 48 h. The collected UV-vis absorption data and dynamic absorption intensity at 267 nm were exported with Cary UV Workstation v.1.2.328 in TXT format. The spectra and dynamic curves were visualized by GraphPad Prism 8.3.0. For TEM and DLS measurements, the concentrations of Na₂SeO₃ and VC were 2.0 and 8.0 mmol L⁻¹, respectively. About 100 μL reaction solution at reaction time points of 5 min, 10 min, 1 h, 4 h, 12 h, and 24 h was dropped onto TEM grids for TEM morphology observation. The size distribution of the reaction mixture was collected immediately once the solutions of VC and Na₂SeO₃ were mixed. The data were measured once every hour for 48 h.

Theoretical calculations

The MD simulation between SeO₃²⁻ or Se atoms on LNT were implemented at a semi-empirical method GFN-xTB (geometry, frequency, noncovalent, extended tight binding).⁴⁴ The GBSA implicit solvation model with water was utilized for water solvation.⁴⁵ The calculations were carried out with the xTB program.⁴⁶ The noncovalent interactions were reflected with an independent gradient model (IGM) analysis.⁴⁷ The data were collected with the aid of Multiwfn 3.8 (dev) software.⁴⁸ The molecular structure visualizations were performed by Visual Molecular Dynamics (VMD) v.1.9.4 software.⁴⁹

ITC measurements of the interactions between Na₂SeO₃ and polysaccharides

The interaction between the polysaccharide and Na₂SeO₃ was analyzed on a MicroCal ITC200 instrument, where a sample cell size of 200 μL and a 300 μL syringe were equipped. The sample cell was filled with 200 μL polysaccharide at a concentration of 4 mg L⁻¹, the reference cell was full of 200 μL ultrapure water, and the experiments were implemented at 25 °C. 20 drops of 40 μL Na₂SeO₃ (4 mmol L⁻¹) were injected into the sample cell within 50 min. The stirring speed was set at 1,000 rpm min⁻¹. The collected data were analyzed and exported by MicroCal PEAQ-ITC Analysis Software. The ITC curves were visualized with GraphPad Prism 8.3.0.

Zeta potential analysis for the mixtures of Na₂SeO₃ and polysaccharides

The measurements were carried out according to the reported literature.⁵⁰ 2.0 mL reaction solution of Na₂SeO₃ (4 mmol L⁻¹) and polysaccharides (LNT, CS, or CMP at 4.0 mg L⁻¹) were subjected to DLS zeta potential analysis (Malvern, NANO ZS) separately. The zeta potentials of different systems were exported with ZETASIZER SOFTWARE v.7.12, and the data were visualized by GraphPad Prism 8.3.0.

Synthesis of SeNPs at laboratory scale

LNT@SeNPs, CS@SeNPs, and CMP@SeNPs were synthesized at laboratory scale in the following procedure: 20 mL of VC (40 mmol L⁻¹) was dropped into 80 mL of Na₂SeO₃ (2.5 mmol L⁻¹, with the presence of 50 mg L⁻¹ different polysaccharides), and the reaction solution was stirred at room temperature for 24 h. After that, the reaction mixture was dialyzed with dialysis sacks (Millipore, D6191, molecular weight cutoff 10 kDa) in ultrapure water for 24 h, and the dialysate was changed every 2 h. The SeNP power was obtained by lyophilization under -20 °C (Labconco Freezone 4.5 L) and stored under room temperature.

Synthesis of SeNPs at pilot scale

The reaction was implemented in a 6 L beaker with 50 mg L⁻¹ LNT following the laboratory-scale procedure. The reaction concentration was 32 mmol L⁻¹ (based on Na₂SeO₃) and was carried out at a 4:1 molar ratio of VC and

Na₂SeO₃. After being stirred at room temperature for 24 h, the reaction mixture was dialyzed using a Millipore Labscale Tangential Flow Filtration (TFF) system, which was equipped with Pellicon XL polyethersulfone membrane (10 kDa). Ultrapure water was used as elution under differential pressures of 20 psi. The purified and concentrated SeNPs were lyophilized under -20 °C (Labconco Freezone 4.5 L).

Synthesis of SeNPs at industrial scale

The large-scale synthesis of LNT@SeNPs (32 mmol L⁻¹ based on Na₂SeO₃) was implemented in a flat panel reactor (Guangzhou enjoyer mechanical equipment, NSG-500), and the prepared SeNPs were dialyzed with an ultrafiltration system (Hefei Shijie Membrane Engineering, SJM-UF-04). Spray drying was performed at the aspirator rate of 60%, flow rate of 600 L/h, pressure of 4.5 bar, feed temperature of 200 °C, and inlet air of 100 °C. Maltodextrin (3% and 5%) was added according to the weight of the SeNPs.

Characterization of SeNPs

The synthesized SeNPs were subjected to DLS (Malvern Zetasizer Nano ZS) for particle size distribution and zeta potential analysis directly. The size distribution was measured at 25 °C. 400 μL of SeNP solution was dropped onto TEM grids, and the samples were observed under TEM (TECNAL G2 Spirit TWIN). Further elemental mapping signal of the SeNPs was collected by high-resolution TEM (JEM-2100F). The UV-vis spectra were recorded under Hitachi UH4150 at wavelengths from 350 to 650 nm.

Long-term stability analysis of SeNPs

The industrial LNT@SeNP powder was kept under ambient conditions for 48 months. LNT@SeNP powder was resuspended in water and the solution (2.5 mmol L⁻¹) were subjected to DLS analysis. The data were exported with ZETASIZER SOFTWARE v.7.12 and visualized by GraphPad Prism 8.3.0. A 400 μL solution of LNT@SeNPs was dropped onto TEM grids, and the morphology of the NPs was observed by TEM after drying naturally. UV-vis spectra were collected by a diluted LNT@SeNP solution. The data were exported and visualized according to procedure described above.

Statistical analysis

All experiments in this study were implemented at least in triplicate and repeated three times, and the collected data were expressed as mean ± SD. The difference between the two groups was assessed with a two-tailed Student's t test, and the difference among multiple groups was analyzed by a one-way ANOVA test.

RESOURCE AVAILABILITY

Lead contact

Further information and requests for resources and reagents should be directed to and will be fulfilled by the lead contact, Tianfeng Chen (tchenf@jnu.edu.cn).

Materials availability

This study did not generate new unique materials. Information about reagents and synthetic procedures used are available in the main text and [supplemental information](#). Any further information needed is available from the [lead contact](#) upon reasonable request.

Data and code availability

All analyzed data are available in the manuscript or [supplemental information](#). This study did not generate/analyze datasets/code. Any further information needed is available from the [lead contact](#) upon reasonable request.

ACKNOWLEDGMENTS

This work was supported by the National Key R&D Program of China (2023YFC3402800), the National Science Fund for Distinguished Young Scholars (82225025), the National Natural Science Foundation of China (32471435, 32171296, 32271351, and 22305096), the Guangdong Basic and

Applied Basic Research Foundation for Distinguished Young Scholars (2024B1515020057), and the Hong Kong Scholars Program (XJ2024048).

AUTHOR CONTRIBUTIONS

L.H. and Z.X. designed the experiments. Z.X., Z.Z., Z.T., C.S., and L.Z. conducted the experiments. K.S. and Z.T. helped to visualize the data. Z.X., L.H., and T.C. wrote, reviewed, edited, and revised the manuscript.

DECLARATION OF INTERESTS

The authors declare no competing interests.

SUPPLEMENTAL INFORMATION

Supplemental information can be found online at <https://doi.org/10.1016/j.xcrp.2024.102303>.

Received: August 5, 2024

Revised: October 9, 2024

Accepted: October 29, 2024

Published: November 25, 2024

REFERENCES

- Hahn, J., Ding, S., Im, J., Harimoto, T., Leong, K.W., and Danino, T. (2024). Bacterial therapies at the interface of synthetic biology and nanomedicine. *Nat. Rev. Bioeng.* 2, 120–135. <https://doi.org/10.1038/s44222-023-00119-4>.
- Xu, R., Cao, H., Lin, D., Yu, B., and Qu, J. (2022). Lanthanide-doped up-conversion nanoparticles for biological super-resolution fluorescence imaging. *Cell Rep. Phys. Sci.* 3, 100922. <https://doi.org/10.1016/j.xcrp.2022.100922>.
- van Vliet, M.T.H., Thorslund, J., Strokal, M., Hofstra, N., Flörke, M., Ehalt Macedo, H., Nkwasa, A., Tang, T., Kaushal, S.S., Kumar, R., et al. (2023). Global river water quality under climate change and hydroclimatic extremes. *Nat. Rev. Earth Environ.* 4, 687–702. <https://doi.org/10.1038/s43017-023-00472-3>.
- de Lázaro, I., and Mooney, D.J. (2021). Obstacles and opportunities in a forward vision for cancer nanomedicine. *Nat. Mater.* 20, 1469–1479. <https://doi.org/10.1038/s41563-021-01047-7>.
- Sousa de Almeida, M., Susnik, E., Drasler, B., Taladriz-Blanco, P., Petri-Fink, A., and Rothen-Rutishauser, B. (2021). Understanding nanoparticle endocytosis to improve targeting strategies in nanomedicine. *Chem. Soc. Rev.* 50, 5397–5434. <https://doi.org/10.1039/D0CS01127D>.
- Huang, Z., Qiu, L., Zhang, T., and Tan, W. (2021). Integrating DNA Nanotechnology with Aptamers for Biological and Biomedical Applications. *Matter* 4, 461–489. <https://doi.org/10.1016/j.matt.2020.11.002>.
- Sun, Z., Ou, Q., Dong, C., Zhou, J., Hu, H., Li, C., and Huang, Z. (2024). Conducting polymer hydrogels based on supramolecular strategies for wearable sensors. *Explorations* 4, 20220167. <https://doi.org/10.1002/EXP.20220167>.
- Ren, Z., Yang, J., Qi, D., Sonar, P., Liu, L., Lou, Z., Shen, G., and Wei, Z. (2021). Flexible Sensors Based on Organic-Inorganic Hybrid Materials. *Adv. Mater. Technol.* 6, 2000889. <https://doi.org/10.1002/admt.202000889>.
- Zhao, T., Meng, D., Hu, Z., Sun, W., Ji, Y., Han, J., Jin, X., Wu, X., and Duan, P. (2023). Enhanced chiroptical properties of nanocomposites of achiral plasmonic nanoparticles decorated with chiral dye-loaded micelles. *Nat. Commun.* 14, 81. <https://doi.org/10.1038/s41467-022-35699-z>.
- Li, L., Shen, Y., Tang, Z., Yang, Y., Fu, Z., Ni, D., and Cai, X. (2023). Engineered nanodrug targeting oxidative stress for treatment of acute kidney injury. *Explorations* 3, 20220148. <https://doi.org/10.1002/EXP.20220148>.
- Fang, R.H., Gao, W., and Zhang, L. (2023). Targeting drugs to tumours using cell membrane-coated nanoparticles. *Nat. Rev. Clin. Oncol.* 20, 33–48. <https://doi.org/10.1038/s41571-022-00699-x>.
- Li, T., and Xu, H. (2020). Selenium-Containing Nanomaterials for Cancer Treatment. *Cell Rep. Phys. Sci.* 1, 100111. <https://doi.org/10.1016/j.xcrp.2020.100111>.
- Kayrouz, C.M., Huang, J., Hauser, N., and Seyedsayamdst, M.R. (2022). Biosynthesis of selenium-containing small molecules in diverse microorganisms. *Nature* 610, 199–204. <https://doi.org/10.1038/s41586-022-05174-2>.
- Bisht, N., Phalswal, P., and Khanna, P.K. (2022). Selenium nanoparticles: a review on synthesis and biomedical applications. *Mater. Adv.* 3, 1415–1431. <https://doi.org/10.1039/D1MA00639H>.
- Mao, L., Wang, L., Zhang, M., Ullah, M.W., Liu, L., Zhao, W., Li, Y., Ahmed, A.A.Q., Cheng, H., Shi, Z., and Yang, G. (2021). In Situ Synthesized Selenium Nanoparticles-Decorated Bacterial Cellulose/Gelatin Hydrogel with Enhanced Antibacterial, Antioxidant, and Anti-Inflammatory Capabilities for Facilitating Skin Wound Healing. *Adv. Healthcare Mater.* 10, 2100402. <https://doi.org/10.1002/adhm.202100402>.
- Ouyang, J., Deng, B., Zou, B., Li, Y., Bu, Q., Tian, Y., Chen, M., Chen, W., Kong, N., Chen, T., and Tao, W. (2023). Oral Hydrogel Microbeads-Mediated In Situ Synthesis of Selenoproteins for Regulating Intestinal Immunity and Microbiota. *J. Am. Chem. Soc.* 145, 12193–12205. <https://doi.org/10.1021/jacs.3c02179>.
- Ferro, C., Florindo, H.F., and Santos, H.A. (2021). Selenium Nanoparticles for Biomedical Applications: From Development and Characterization to Therapeutics. *Adv. Healthcare Mater.* 10, 2100598. <https://doi.org/10.1002/adhm.202100598>.
- Nabi, F., Arain, M.A., Hassan, F., Umar, M., Rajput, N., Alagawany, M., Syed, S.F., Soomro, J., Somroo, F., and Liu, J. (2020). Nutraceutical role of selenium nanoparticles in poultry nutrition: a review. *World's Poult. Sci. J.* 76, 459–471. <https://doi.org/10.1080/00439339.2020.1789535>.
- Garza-García, J.J.O., Hernández-Díaz, J.A., Zamudio-Ojeda, A., León-Morales, J.M., Guerrero-Guzmán, A., Sánchez-Chiprés, D.R., López-Velázquez, J.C., and García-Morales, S. (2022). The Role of Selenium Nanoparticles in Agriculture and Food Technology. *Biol. Trace Elem. Res.* 200, 2528–2548. <https://doi.org/10.1007/s12111-021-02847-3>.
- Shang, H., Li, C., Cai, Z., Hao, Y., Cao, Y., Jia, W., Han, L., White, J.C., Ma, C., and Xing, B. (2024). Biosynthesized Selenium Nanoparticles as an Effective Tool to Combat Soil Metal Stresses in Rice (*Oryza sativa* L.). *ACS Nano* 18, 19636–19648. <https://doi.org/10.1021/acsnano.4c04215>.
- Salama, H.H., El-Sayed, H.S., Abd-Rabou, N.S., and Hassan, Z.M.R. (2021). Production and use of eco-friendly selenium nanoparticles in the fortification of yoghurt. *J. Food Process. Preserv.* 45, e15510. <https://doi.org/10.1111/jfpp.15510>.
- Wang, K., Wang, Y., Li, K., Wan, Y., Wang, Q., Zhuang, Z., Guo, Y., and Li, H. (2020). Uptake, translocation and biotransformation of selenium nanoparticles in rice seedlings (*Oryza sativa* L.). *J. Nanobiotechnol.* 18, 103. <https://doi.org/10.1186/s12951-020-00659-6>.
- Hargreaves, I.P., and Mantle, D. (2019). Supplementation with selenium and coenzyme Q10 in critically ill patients. *Br. J. Hosp. Med.* 80, 589–593. <https://doi.org/10.12968/hmed.2019.80.10.589>.
- Zhang, X., Chen, X., Guo, Y., Gu, L., Wu, Y., Bindra, A.K., Teo, W.L., Wu, F.-G., and Zhao, Y. (2021). Thiolate-Assisted Route for Constructing Chalcogen Quantum Dots with Photoinduced Fluorescence Enhancement. *ACS Appl. Mater. Interfaces* 13, 48449–48456. <https://doi.org/10.1021/acsami.1c15772>.
- Hashem, A.H., and Salem, S.S. (2022). Green and ecofriendly biosynthesis of selenium nanoparticles using *Urtica dioica* (stinging nettle) leaf extract: Antimicrobial and anticancer activity. *Biotechnol. J.* 17, 2100432. <https://doi.org/10.1002/biot.202100432>.
- Huang, Y., Fu, Y., Li, M., Jiang, D., Kutyreff, C.J., Engle, J.W., Lan, X., Cai, W., and Chen, T. (2020). Chirality-Driven Transportation and Oxidation

- Prevention by Chiral Selenium Nanoparticles. *Angew Chem. Int. Ed. Engl.* 59, 4406–4414. <https://doi.org/10.1002/anie.201910615>.
27. Huang, W., Wang, M., Hu, L., Wang, C., Xie, Z., and Zhang, H. (2020). Recent Advances in Semiconducting Monoelemental Selenium Nanostructures for Device Applications. *Adv. Funct. Mater.* 30, 2003301. <https://doi.org/10.1002/adfm.202003301>.
 28. Diko, C.S., Zhang, H., Lian, S., Fan, S., Li, Z., and Qu, Y. (2020). Optimal synthesis conditions and characterization of selenium nanoparticles in *Trichoderma* sp. WL-Go culture broth. *Mater. Chem. Phys.* 246, 122583. <https://doi.org/10.1016/j.matchemphys.2019.122583>.
 29. Peng, X., Ai, F., Yan, L., Ha, E., Hu, X., He, S., and Hu, J. (2021). Synthesis strategies and biomedical applications for doped inorganic semiconductor nanocrystals. *Cell Rep. Phys. Sci.* 2, 100436. <https://doi.org/10.1016/j.xcrp.2021.100436>.
 30. Jiang, R., Da, Y., Han, X., Chen, Y., Deng, Y., and Hu, W. (2021). Ultrafast Synthesis for Functional Nanomaterials. *Cell Rep. Phys. Sci.* 2, 100302. <https://doi.org/10.1016/j.xcrp.2020.100302>.
 31. Qin, L., Gan, J., Niu, D., Cao, Y., Duan, X., Qin, X., Zhang, H., Jiang, Z., Jiang, Y., Dai, S., et al. (2022). Interfacial-confined coordination to single-atom nanotherapeutics. *Nat. Commun.* 13, 91. <https://doi.org/10.1038/s41467-021-27640-7>.
 32. Rahaman, S.M., Bardhan, A., Mandal, T., Chakraborty, M., Karmakar, K., Dhibar, S., Sharma, S., Chakravarty, M., Ibrahim, S.M., and Saha, B. (2023). Understanding the effect of surfactants' hydrophobicity on the growth of lanthanum sulfide nanospheres in water-in-oil microemulsions: a detailed dynamic light scattering, small angle X-ray scattering, and microscopy study. *New J. Chem.* 47, 10309–10321. <https://doi.org/10.1039/D3NJ00935A>.
 33. Rahaman, S.M., Khatun, N., Pal, P., Mandal, T., Patra, A., Nandi, M., and Saha, B. (2024). A deeper insight into the evaluation of water-in-oil amicroemulsion templated samarium sulfide nanospheres: exploring its role in pickering emulsion formulation for photocatalytic dye degradation and synthesis of PANI@Sm₂S₃ nanocomposites. *Nanoscale Adv.* 6, 1688–1703. <https://doi.org/10.1039/D3NA01067H>.
 34. Lee, D., Huntoon, K., Lux, J., Kim, B.Y.S., and Jiang, W. (2023). Engineering nanomaterial physical characteristics for cancer immunotherapy. *Nat. Rev. Bioeng.* 1, 499–517. <https://doi.org/10.1038/s44222-023-00047-3>.
 35. Li, K., Li, J., Zhang, S., Zhang, J., Xu, Q., Xu, Z., and Guo, Y. (2024). Amorphous structure and crystal stability determine the bioavailability of selenium nanoparticles. *J. Hazard Mater.* 465, 133287. <https://doi.org/10.1016/j.hazmat.2023.133287>.
 36. Wan, J., Wang, J., Guo, H., Wan, K., Zhao, X., Li, J., Li, S., Chen, Z., Liu, S., and Zhang, K. (2022). Constructing ultra-stable photothermal plastics assisted by carbon dots with photocaged reactivity. *Matter* 5, 2864–2881. <https://doi.org/10.1016/j.matt.2022.05.036>.
 37. Luo, C., He, L., Chen, F., Fu, T., Zhang, P., Xiao, Z., Liu, Y., and Tan, W. (2021). Stimulus-responsive nanomaterials containing logic gates for biomedical applications. *Cell Rep. Phys. Sci.* 2, 100350. <https://doi.org/10.1016/j.xcrp.2021.100350>.
 38. Ma, Y., Wang, J., Yu, J., Zhou, J., Zhou, X., Li, H., He, Z., Long, H., Wang, Y., Lu, P., et al. (2021). Surface modification of metal materials for high-performance electrocatalytic carbon dioxide reduction. *Matter* 4, 888–926. <https://doi.org/10.1016/j.matt.2021.01.007>.
 39. Han, D., Wang, J., Zheng, T., Peng, L., and Jiao, T. (2023). Supramolecular assembly with stimuli-responsive circularly polarized luminescence. *Cell Rep. Phys. Sci.* 4, 101523. <https://doi.org/10.1016/j.xcrp.2023.101523>.
 40. Shen, K., Zhang, Y., Wang, X., Ou, C., Guo, F., Zhu, H., Liu, C., Gao, Y., Schropp, R.E.I., Li, Z., et al. (2020). Efficient and Stable Planar n-i-p Sb₂Se₃ Solar Cells Enabled by Oriented 1D Trigonal Selenium Structures. *Adv. Sci.* 7, 2001013. <https://doi.org/10.1002/advs.202001013>.
 41. Li, J., and Deepak, F.L. (2022). In Situ Kinetic Observations on Crystal Nucleation and Growth. *Chem. Rev.* 122, 16911–16982. <https://doi.org/10.1021/acs.chemrev.1c01067>.
 42. Chen, G., Gibson, K.J., Liu, D., Rees, H.C., Lee, J.-H., Xia, W., Lin, R., Xin, H.L., Gang, O., and Weizmann, Y. (2019). Regioselective surface encoding of nanoparticles for programmable self-assembly. *Nat. Mater.* 18, 169–174. <https://doi.org/10.1038/s41563-018-0231-1>.
 43. Troyano, J., Çamur, C., Garzón-Tovar, L., Carné-Sánchez, A., Imaz, I., and Maspoch, D. (2020). Spray-Drying Synthesis of MOFs, COFs, and Related Composites. *Acc. Chem. Res.* 53, 1206–1217. <https://doi.org/10.1021/acs.accounts.0c00133>.
 44. Grimme, S., Bannwarth, C., and Shushkov, P. (2017). A Robust and Accurate Tight-Binding Quantum Chemical Method for Structures, Vibrational Frequencies, and Noncovalent Interactions of Large Molecular Systems Parametrized for All spd-Block Elements (Z = 1–86). *J. Chem. Theor. Comput.* 13, 1989–2009. <https://doi.org/10.1021/acs.jctc.7b00118>.
 45. Ehlert, S., Stahn, M., Spicher, S., and Grimme, S. (2021). Robust and Efficient Implicit Solvation Model for Fast Semiempirical Methods. *J. Chem. Theor. Comput.* 17, 4250–4261. <https://doi.org/10.1021/acs.jctc.1c00471>.
 46. Bannwarth, C., Caldeweyher, E., Ehlert, S., Hansen, A., Pracht, P., Seibert, J., Spicher, S., and Grimme, S. (2021). Extended tight-binding quantum chemistry methods. *WIREs Comput. Mol. Sci.* 11, e1493. <https://doi.org/10.1002/wcms.1493>.
 47. Lefebvre, C., Rubez, G., Khatabil, H., Boisson, J.C., Contreras-García, J., and Hénon, E. (2017). Accurately extracting the signature of intermolecular interactions present in the NCI plot of the reduced density gradient versus electron density. *Phys. Chem. Chem. Phys.* 19, 17928–17936. <https://doi.org/10.1039/C7CP02110K>.
 48. Lu, T., and Chen, F. (2012). Multiwfn: A multifunctional wavefunction analyzer. *J. Comput. Chem.* 33, 580–592. <https://doi.org/10.1002/jcc.22885>.
 49. Humphrey, W., Dalke, A., and Schulter, K. (1996). VMD: Visual molecular dynamics. *J. Mol. Graph.* 14, 33–38. [https://doi.org/10.1016/0263-7855\(96\)00018-5](https://doi.org/10.1016/0263-7855(96)00018-5).
 50. Rahaman, S.M., Chakraborty, M., Kundu, S., Dhibar, S., Kumar, D., Ibrahim, S.M., Chakravarty, M., and Saha, B. (2023). Controlled synthesis of samarium trifluoride nanoparticles in a water-in-oil microemulsion: Effects of water-to-surfactant ratio on particles and phosphate removal. *J. Hazard. Mater.* 11, 100348. <https://doi.org/10.1016/j.hazadv.2023.100348>.